

## Microtesla MRI of the human brain combined with MEG

Vadim S. Zotev, Andrei N. Matlashov, Petr L. Volegov, Igor M. Savukov,  
Michelle A. Espy, John C. Mosher, John J. Gomez & Robert H. Kraus, Jr

Los Alamos National Laboratory, Applied Modern Physics Group, MS D454,  
Los Alamos, NM 87545, USA. E-mail: [vzotev@lanl.gov](mailto:vzotev@lanl.gov)

**Abstract** - Detailed understanding of human brain function requires the ability to non-invasively image brain activity with both high temporal and high spatial resolution. Presently, this can only be achieved through integration of complementary imaging modalities, such as magnetoencephalography (MEG) [1] and magnetic resonance imaging (MRI)[2] or functional MRI (fMRI) [3,4]. MEG, which uses highly sensitive superconducting quantum interference devices (SQUIDS) [5] to directly measure magnetic fields of neuronal currents, cannot be combined with conventional high-field MRI in a single instrument. MEG and MRI data, acquired by two different systems, can only be matched indirectly, by means of an elaborate and error-prone co-registration [6]. A new imaging method – SQUID-based microtesla MRI [7] – can be naturally combined with MEG in the same system to provide an anatomical map for MEG-localized neural sources. Here we report the first MR images of the human brain acquired at a microtesla-range measurement field, together with auditory MEG (functional) data, recorded using the same seven-channel SQUID system during the same imaging session. This result demonstrates feasibility and potential of human brain imaging by microtesla MRI. It also shows that two new types of imaging equipment – systems for anatomical MRI of the human brain at microtesla fields, and more advanced instruments for combined functional (MEG) and structural (microtesla MRI) brain imaging – are practical. Information provided by such combined instruments can be easily integrated with data from other imaging modalities, including fMRI, to utilize advantages of different methods and enable high-resolution spatiotemporal imaging of brain function.

Submitted February 5, 2008. Accepted February 7, 2008. ; Reference No. ST31; Category: 4. A letter version of this article is submitted for publication and available at <http://arxiv.org/abs/0711.0222>.

### I. INTRODUCTION

No single noninvasive imaging modality used to study human brain can, at present, provide comprehensive information about brain function. MEG and electroencephalography (EEG) measure the direct consequences of neuronal activity with millisecond temporal resolution, but their source localization accuracy is limited due to the ill-posed nature of the electromagnetic inverse problem. Moreover, these methods cannot image brain anatomical structure, which is usually obtained by a separate MRI. Functional MRI can provide high spatial resolution, but its temporal resolution is limited by the natural slowness of the hemodynamic response. Moreover, the relationship between such response and neuronal activity is not yet fully understood [8]. Integration of imaging modalities [9], for example, the combination of fMRI with MEG [10] or EEG [11], is commonly viewed as an approach to realize high-resolution

spatiotemporal imaging of brain function. However, high magnetic fields and intense rf pulses used in conventional MRI make any such integration extremely difficult. While simultaneous acquisition of EEG and fMRI signals is technically challenging [11], combination of MEG and MRI (or fMRI) in a single instrument is beyond current technological capabilities. An elaborate co-registration procedure, presently required to merge MEG and MRI data from different instruments, introduces errors on the order of 5-10 mm [6], which exceed average MEG source localization errors [12] and make MEG less efficient as a pre-surgical evaluation tool.

## II. MICROTESLA FIELD MRI

Magnetic resonance imaging at microtesla fields [7], also referred to as ultralow-field (ULF) MRI, uses the same type of magnetic sensors as those used for MEG (SQUIDs with untuned input circuits). Earlier work by our group demonstrated that MEG and ULF NMR signals (that provide the basis for ULF MRI) could be detected simultaneously by the same SQUID [13]. The ULF-MRI method relies on the well-known pre-polarization technique [14] to increase an object's magnetization prior to each imaging step performed at a microtesla-range measurement field. In contrast to high-field MRI, relative homogeneity of the measurement field is not crucial in ULF MRI, because microtesla-range magnetic fields of even modest relative homogeneity are highly homogeneous on the absolute scale [15]. Microtesla MRI holds three important promises for medical imaging in general, and neuroimaging in particular. First, imaging at ULF can be performed using simple and inexpensive coil systems of open geometry [16,17], that do not subject human brain to strong magnetic fields and rf pulses, and allow imaging in the presence of metal [18]. Second,  $T_1$ -weighted contrast is, in some cases, improved at low fields [19], allowing one to more efficiently identify various medical conditions that affect  $T_1$ , such as brain tumors [20]. Third, microtesla MRI can be combined with MEG and other SQUID-based techniques for biomagnetic measurements [13,21]. This allows development of new medical instruments, such as multichannel SQUID systems for both functional (MEG) and structural (ULF MRI) imaging [22] of the human brain. In a parallel effort, existing whole-head MEG systems can be modified [23] to include ULF MRI capability. No co-registration of MEG and ULF MRI data is required with such combined systems after spatial sensitivities of MEG sensors were mapped by ULF MRI during an initial uniform-phantom calibration. Because ULF images can be precisely matched to structural images provided by other imaging modalities, ULF MRI can enable seamless integration of MEG and EEG, on the one hand, with high-spatial-resolution MRI and fMRI, on the other.

## III. MEASURING SYSTEM AND PROCEDURE

The brain imaging results reported in this Letter were obtained using the experimental system [17] and procedure, depicted schematically in Figure 1. The system includes seven second-order SQUID gradiometers with magnetic field resolution of 1.2 to 2.8 fT/ $\sqrt{\text{Hz}}$ , installed inside a flat-bottom non-metallic (fibreglass) liquid helium cryostat in a pattern shown in (a). The cryostat is mounted inside an open-type coil system (b) that generates magnetic fields and gradients for ULF MRI according to the sequence shown in (c). The system is operated inside a magnetically shielded room. The ULF images were acquired at the measurement field  $B_m = 46 \mu\text{T}$ , corresponding to

the proton Larmor frequency of 1940 Hz. A stronger pre-polarizing field  $B_p=30$  mT perpendicular to  $B_m$  was applied for 1 s prior to each imaging step, and was removed before the application of  $B_m$ . The imaging sequence (c) was based on the 3D Fourier protocol and provided images with  $3 \text{ mm} \times 3 \text{ mm} \times 6 \text{ mm}$  spatial resolution. To study transverse relaxation properties of brain tissues, we implemented a modification of the commonly used multiple-echo technique [24]. Each of the four echoes acquired (c) was induced by simultaneous reversal of the measurement field  $B_m$  [16] and the readout gradient  $G_x$  to compensate for spatial inhomogeneities of both.

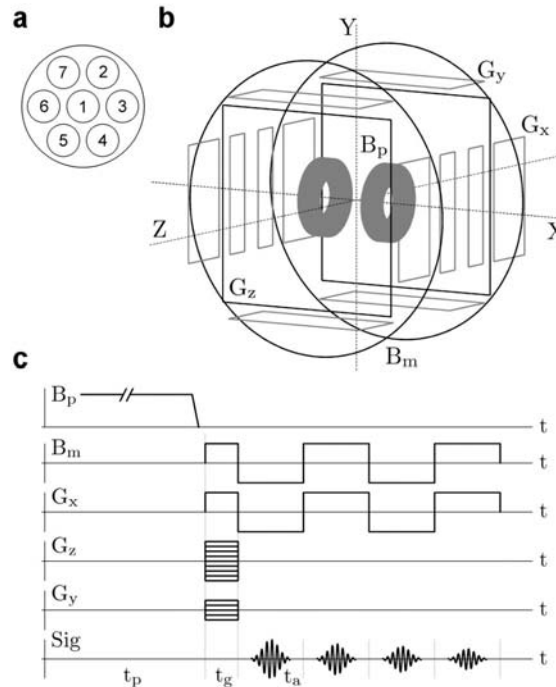


**Figure 1.** Experimental set-up and procedure for multi-echo 3D ULF MRI. (a) Positions of the seven SQUID gradiometers inside the liquid He cryostat. The gradiometers have 37 mm diameter, 60 mm baseline, and 45 mm center-to-center spacing for the neighboring coils; (b) Schematic layout of the coil system for 3D Fourier imaging with pre-polarization. Notations:  $B_p$  – pre-polarizing field,  $B_m$  – measurement field,  $G_x=dB_z/dx$  – frequency encoding gradient,  $G_z=dB_z/dz$  and  $G_y=dB_z/dy$  – phase encoding gradients. Each of the five sets of coils is symmetric with respect to the system center. The largest coils ( $B_m$ ) are 120 cm in diameter. (c) Multiple-echo imaging sequence. Physical parameters:  $B_p=30$  mT,  $B_m=\pm 46$   $\mu$ T,  $G_x=\pm 140$   $\mu$ T/m,  $G_z=\pm 140$   $\mu$ T/m limits, 61 steps,  $G_y=\pm 70$   $\mu$ T/m limits, 11 steps,  $t_p=1$  s,  $t_g=28$  ms, and  $t_a=56$  ms. *Sig* – echo signals measured by a SQUID. The four echoes attain maxima at  $TE = 63, 142, 205,$  and  $283$  ms, respectively, measured from the moment  $B_m$  is first applied.

#### IV. RESULTS

Figures 2 and 3 show images of the human head we acquired at ULF. It may be instructive to compare them to brain images produced by early MRI [25]. Two separate experiments were performed, in which the right side of the head and the forehead area were imaged using the protocol described above (see also the caption of Figure 1). Six consecutive scans of the phase space were completed, and the resulting 3D images were averaged ( $N = 6$ ) for each channel. Each ULF image in Figures 2 and 3 is a composite

image computed as a square root of the sum of squares of images from the seven individual channels. Each image was also subjected to fine-mesh interpolation and correction of concomitant gradient artifacts [26]. Only four horizontal image layers (out of 11 simultaneously acquired) are shown in Figure 2. The total imaging time was about 90 minutes in each experiment, with 75% of this time taken up by pre-polarization. We expect imaging resolution and speed to increase substantially as we improve performance of the system and use stronger pre-polarizing fields. We also intend to increase sensitivity depth by using larger pick-up coils.

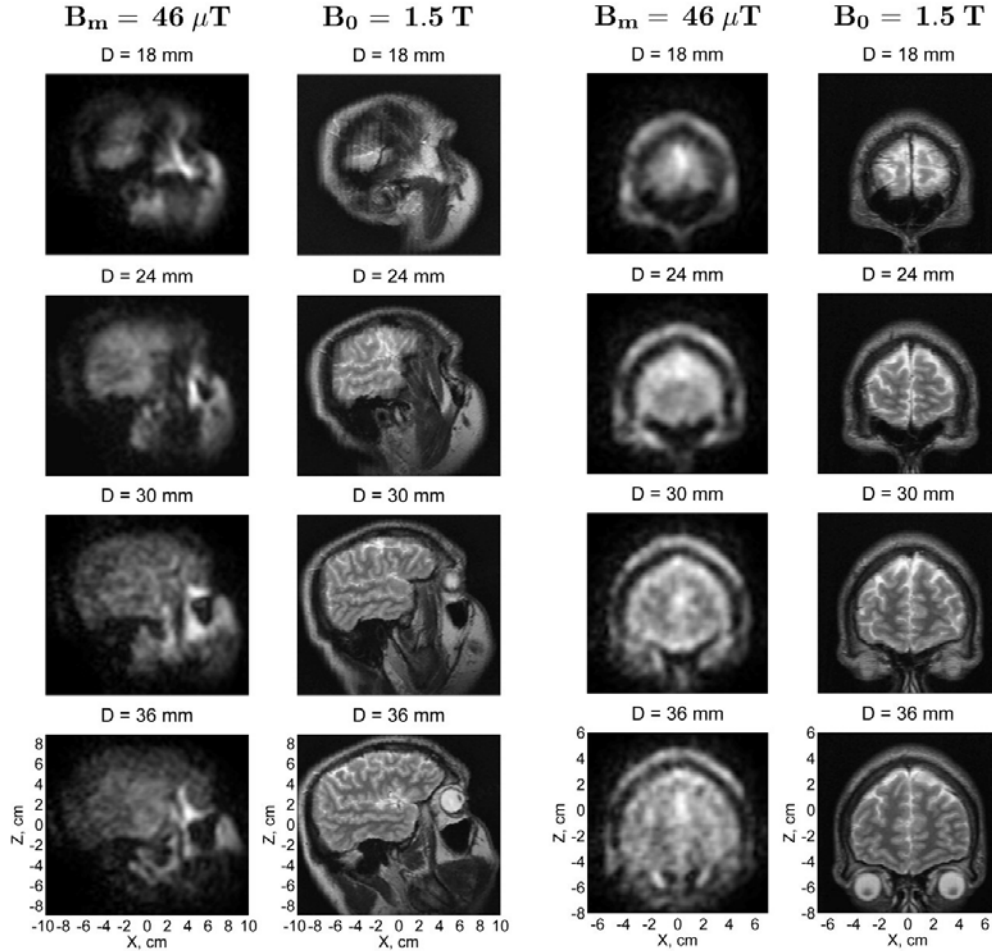


**Figure 2.** Microtesla MRI of the human head compared to high-field MRI. The 3D ULF MR images of the head side and the forehead area were acquired at  $B_m=46 \mu\text{T}$  measurement field with pre-polarization at 30 mT. The in-plane resolution is  $3 \text{ mm} \times 3 \text{ mm}$ . Each image represents a 6 mm-thick layer of the head.  $D$  is the depth of the central plane of a given layer with respect to the bottom of the cryostat. The images correspond to the first echo with  $TE=63 \text{ ms}$ . The pre-polarization time was 1 s for each imaging step. The high-field 3D image of the same subject's head was acquired by conventional MRI at  $B_0=1.5 \text{ T}$  with  $TE=64 \text{ ms}$  and  $TR=9000 \text{ ms}$ . The image, originally with 1 mm isotropic resolution, was subjected to rotation and summation over depth within 6 mm-thick layers to approximately match each of the two 3D ULF MR images.

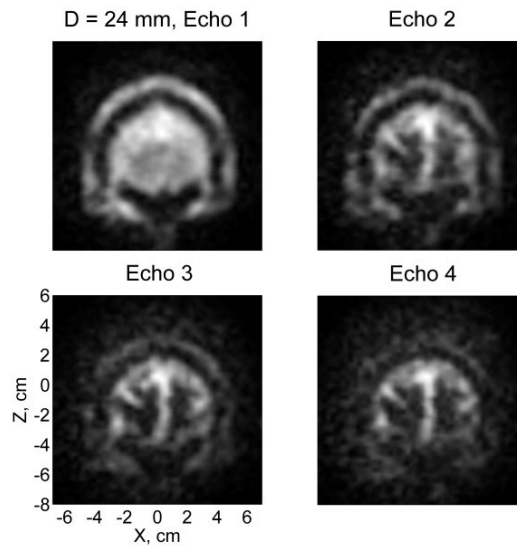


**Figure 3.**  $T_2$ -weighted contrast in microtesla MRI of the human head. The four images of the same 6 mm-thick layer, acquired at 46  $\mu\text{T}$  measurement field, correspond to four echoes with echo times  $TE=63$ , 142, 205, and 283 ms. The contrast between brain tissues and CSF improves visibly with echo time.

The ULF images in Figure 2 correspond to the first echo. Brain tissues (gray and white matter) in these images have approximately the same brightness as cerebrospinal fluid (CSF), which can be explained as follows. Because the pre-polarization time  $t_p=1$  s is longer than any  $T_1$  values in the brain (for white matter,  $T_1=200$  ms was reported at 20 mT field [27]), but shorter than  $T_1$  of CSF, hence, the initial polarization of brain tissues is higher than that of CSF. However, we found that  $T_2$  for CSF is longer at 46  $\mu\text{T}$  than  $T_2$  for gray and white matter, as shown below. Thus, the brain in our experiments should look brighter at shorter echo times, while the CSF is brighter at longer  $TE$ 's. The latter tendency is observed in Figure 3, which shows different degrees of  $T_2$ -weighted contrast at 46  $\mu\text{T}$  field. Clearly, further studies of relaxation times at ULF are indicated and may ultimately lead to important new contrast mechanisms.

Using multiple-echo data we estimated  $T_2$  values for different human tissues for the first time at ULF. Identification of tissues was based on a detailed comparison of ULF images with high-field images of the same head (Fig. 2), together with analysis of their long-time relaxation (Fig. 3). Image intensities for 10-20 pixels corresponding to a certain tissue type were then averaged for each echo, and a single exponential function was fitted to the resulting data. The error bars below represent standard deviations of the respective fits. For gray and white matter,  $T_2$  values at 46  $\mu\text{T}$  were found to be  $106\pm 11$  ms and  $79\pm 11$  ms, respectively. The relaxation is slower for CSF, with  $T_2 = 355\pm 15$  ms. Other  $T_2$  values easily determined from our data are  $120\pm 7$  ms for scalp,  $102\pm 5$  ms for maxillary sinuses,  $108\pm 2$  ms for soft tissues around eyes, and  $667\pm 23$  ms for eyeballs. In each case, the same analysis was also applied to images of a large uniform water phantom, and relaxation times longer than 1400 ms were invariably obtained. This means that  $T_2$  values determined in this work are reliable, and not shortened drastically by field inhomogeneities. Based on our results, we conclude that  $T_2$  values for gray and white matter at 46  $\mu\text{T}$  are close to those measured in high-field MRI. At 3T field, for

example,  $T_2=110$  ms and 80 ms for gray and white matter, respectively [28]. This agrees with earlier observations that  $T_2$  is essentially independent of the magnetic field strength [20,28]. Further and more extensive studies of transverse relaxation at ULF are required because of the important medical role played by  $T_2$ -weighted contrast.

Auditory MEG measurements shown in Figure 4 were performed immediately after the ULF MRI of the right side of the head (Fig. 2), while the human subject remained inside the system. The head, originally positioned to ensure coverage of important anatomical features by the system's channels (Ch 1 above the temple, Ch 3 above the eye, Fig. 1(a)), was moved slightly to increase coverage of the auditory cortex (Ch 1 above the ear, Ch 3 above the temple). Such head repositioning would not be necessary with a whole-head SQUID array typically used in MEG. Each auditory evoked response curve in Fig. 4, obtained as an average of 200 digitally filtered measurements, exhibits a series of peaks characteristic of auditory MEG [1]. These results demonstrate that our system can be used for both ULF MRI of the brain and magnetoencephalography.

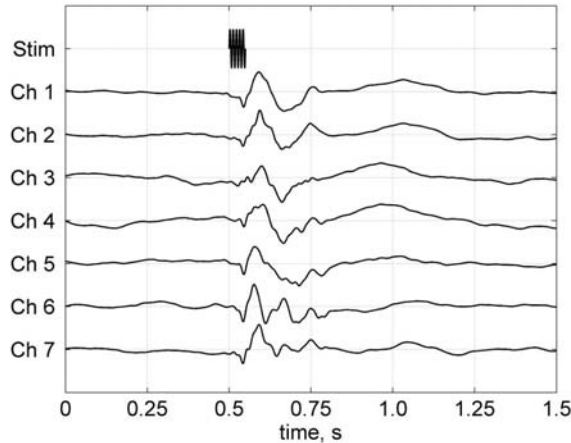


**Figure 4.** Auditory MEG recordings with the same system. The stimulus consisted of a 50 ms long 1 kHz tone pulse, with 500 ms pre-stimulus interval and 1500 ms post-stimulus interval. The auditory evoked response curves have peak-to-peak magnitudes of 237, 132, 81, 78, 95, 149, and 239 fT for channels 1 through 7, respectively. They are normalized by one in the figure to emphasize their time dependence.

## V. CONCLUSION AND OUTLOOK

While the imaging resolution at ULF reported here is not high, it allows 3D matching of ULF images (and any related MEG data) to high-field MR images of the same head with far better accuracy than that of the traditional MEG/MRI co-registration [6]. This shows potential of ULF MRI as a multimodal integration tool.

The results reported here, together with the other results in this field, suggest that SQUID-based microtesla MRI is becoming a new brain imaging modality with its own unique opportunities and challenges. Its further development should exploit its natural advantages, and include significant, but low-cost improvement in imaging resolution

and speed, investigation of clinical benefits of enhanced  $T_1$  (and possibly  $T_2$ ) contrast, and design of whole-head MEG/ULF-MRI systems.

### ACKNOWLEDGEMENTS

The authors gratefully acknowledge the support of the U.S. National Institutes of Health (Grant No. R01-EB006456), and the U.S. Department of Energy OBER (Grant No. KP150302, project ERWS115). We also thank Dr. Diana South of Mind Research Network (Albuquerque, NM) for performing 1.5T and 3T brain scans of our human subject.

### REFERENCES

- [1] Hämäläinen, M., Hari, R., Ilmoniemi, R. J., Knuutila, J. & Lounasmaa, O. V. Magnetoencephalography – theory, instrumentation, and applications to noninvasive studies of the working human brain. *Rev. Mod. Phys.* **65**, 413-497 (1993).
- [2] Lauterbur, P. C. Image formation by induced local interactions: examples employing nuclear magnetic resonance. *Nature* **242**, 190–191 (1973).
- [3] Belliveau, J. W., Kennedy, D. N., McKinstry, R. C., Buchbinder, B. R., Weisskoff, R. M., Cohen, M. S., Vevea, J. M., Brady, T. J. & Rosen, B. R. Functional mapping of the human visual cortex by magnetic resonance imaging. *Science* **254**, 716-719 (1991).
- [4] Ogawa, S., Tank, D. W., Menon, R., Ellermann, J. M., Kim, S.-G., Merkle, H. & Ugurbil, K. Intrinsic signal changes accompanying sensory stimulation: functional brain mapping with magnetic resonance imaging. *Proc. Natl. Acad. Sci. USA* **89**, 5951-5955 (1992).
- [5] Clarke, J. & Braginski, A. I. (Eds.) *The SQUID Handbook* (Wiley-VCH, Weinheim, 2004).
- [6] Adjarian, P., Barnes, G. R., Hillebrand, A., Holliday, I. E., Singh, K. D., Furlong, P. L., Harrington, E., Barclay, C. W. & Route, P. J. G. Co-registration of magnetoencephalography with magnetic resonance imaging using bite-bar-based fiducials and surface-matching. *Clin. Neurophysiol.* **115**, 691-698 (2004).
- [7] McDermott, R., Lee, S.-K., ten Haken, B., Trabesinger, A. H., Pines, A. & Clarke, J. Microtesla MRI with a superconducting quantum interference device. *Proc. Natl. Acad. Sci. USA* **101**, 7857-7861 (2004).
- [8] Mukamel, R., Gelbard, H., Arieli, A., Hasson, U., Fried, I. & Malach, R. Coupling between neuronal firing, field potentials, and fMRI in human auditory cortex. *Science* **309**, 951-954 (2005).
- [9] Dale, A. M. & Halgren, E. Spatiotemporal mapping of brain activity by integration of multiple imaging modalities. *Curr. Opin. Neurobiol.* **11**, 202-208 (2001).
- [10] Ahlfors, S. P., Simpson, G. V., Dale, A. M., Belliveau, J. W., Liu, A. K., Korvenoja, A., Virtanen, J., Huotilainen, M., Tootell, R. B. H., Aronen, H. J. & Ilmoniemi, R. J. Spatiotemporal activity of a cortical network for processing visual motion revealed by MEG and fMRI. *J. Neurophysiol.* **82**, 2545-2555 (1999).
- [11] Goldman, R. I., Stern, J. M., Engel Jr., J. & Cohen, M. S. Acquiring simultaneous EEG and functional MRI. *Clin. Neurophysiol.* **111**, 1974-1980 (2000).
- [12] Leahy, R. M., Mosher, J. C., Spencer, M. E., Huang, M. X. & Lewine, J. D. A study of dipole localization accuracy for MEG and EEG using a human skull phantom. *Electroenceph. Clin. Neurophysiol.* **107**, 159-173 (1998).

- [13] Volegov, P., Matlachov, A. N., Espy M. A., George J. S. & Kraus, Jr., R. H. Simultaneous magnetoencephalography and SQUID detected nuclear MR in microtesla magnetic fields. *Magn. Reson. Med.* **52**, 467-470 (2004).
- [14] Macovski, A. & Conolly, S. Novel approaches to low-cost MRI. *Magn. Reson. Med.* **30**, 221-230 (1993).
- [15] McDermott, R., Trabesinger, A. H., Mück M., Hahn, E. L., Pines, A. & Clarke J. Liquid-state NMR and scalar couplings in microtesla magnetic fields. *Science* **295**, 2247-2249 (2002).
- [16] McDermott, R., Kelso, N., Lee, S.-K., Mößle, M., Mück, M., Myers, W., ten Haken, B., Seton, H. C., Trabesinger, A. H., Pines, A. & Clarke, J. SQUID-detected magnetic resonance imaging in microtesla magnetic fields. *J. Low Temp. Phys.* **135**, 793-821 (2004).
- [17] Zotev, V. S., Matlashov, A. N., Volegov, P. L., Urbaitis, A. V., Espy, M. A. & Kraus, Jr., R. H. SQUID-based instrumentation for ultralow-field MRI. *Supercond. Sci. Technol.* **20**, S367-S373 (2007).
- [18] Mößle, M., Han, S.-I., Myers, W. R., Lee S.-K., Kelso, N., Hatridge, M., Pines, A. & Clarke, J. SQUID-detected microtesla MRI in the presence of metal. *J. Magn. Reson.* **179**, 146-151 (2006).
- [19] Lee, S.-K., Mößle, M., Myers, W., Kelso, N., Trabesinger, A. H., Pines, A. & Clarke, J. SQUID-detected MRI at 132  $\mu$ T with  $T_1$ -weighted contrast established at 10  $\mu$ T-300 mT. *Magn. Reson. Med.* **53**, 9-14 (2005).
- [20] Bottomley, P. A., Hardy, C. J., Argersinger, R. E. & Allen-Moore, G. A review of  $^1\text{H}$  nuclear magnetic resonance relaxation in pathology: are  $T_1$  and  $T_2$  diagnostic? *Med. Phys.* **14**, 1-37 (1987).
- [21] Espy, M. A., Matlachov, A. N., Volegov, P. L., Mosher, J. C. & Kraus, Jr., R. H. SQUID-based simultaneous detection of NMR and biomagnetic signals at ultra-low magnetic fields. *IEEE Trans. Appl. Supercond.* **15**, 635-639 (2005).
- [22] Zotev, V. S., Matlachov, A. N., Volegov, P. L., Sandin, H. J., Espy, M. A., Mosher, J. C., Urbaitis, A. V., Newman, S. G. & Kraus, Jr., R. H. Multi-channel SQUID system for MEG and ultra-low-field MRI. *IEEE Trans. Appl. Supercond.* **17**, 839-842 (2007).
- [23] Burghoff, M., Hartwig, S., Kilian, W., Vorwerk, A. & Trahms, L. SQUID systems adapted to record nuclear magnetism in low magnetic fields. *IEEE Trans. Appl. Supercond.* **17**, 846-849 (2007).
- [24] Poon, C. S. & Henkelman, R. M. Practical  $T_2$  quantitation for clinical applications. *J. Magn. Reson. Imaging* **2**, 541-553 (1992).
- [25] Moore, W. S., Holland, G. N. & Kreel, L. The NMR CAT scanner – a new look at the brain. *J. Comput. Assist. Tomogr.* **4**, 1-7 (1980).
- [26] Myers, W. R., Mößle, M. & Clarke, J. Correction of concomitant gradient artifacts in experimental microtesla MRI. *J. Magn. Reson.* **177**, 274-284 (2005).
- [27] Agartz, I., Sääf, J., Wahlund, L. O. & Wetterberg, L.  $T_1$  and  $T_2$  relaxation time estimates in the normal human brain. *Radiology* **181**, 537-543 (1991).
- [28] Wansapura, J. P., Holland, S. K., Dunn, R. S. & Ball, W. S., Jr. NMR relaxation times in the human brain at 3.0 Tesla. *J. Magn. Reson. Imaging* **9**, 531-538 (1999).